Stability Analysis of a Predictor/Multi-corrector Method for Staggered-Grid Lagrangian Shock Hydrodynamics☆

E. Love[a], W. J. Rider[a], G. Scovazzi[a,*]

[a] *1431 Computational Shock- and Multi-physics Department, Sandia National Laboratories, P.O. Box 5800, MS 1319, Albuquerque, NM 87185-1319, USA*

Abstract

This article presents the complete von Neumann stability analysis of a predictor/multi-corrector scheme derived from an implicit mid-point time integrator often used in shock hydrodynamics computations in combination with staggered spatial discretizations. It is shown that only even iterates of the method yield stable computations, while the odd iterates are, in the most general case, unconditionally unstable. Dispersion error analysis is also presented.

Key words: von Neumann stability analysis, predictor/multi-corrector algorithm, mid-point time integrator, Lagrangian shock hydrodynamics, staggered formulation.

1. Introduction

The present article proposes a complete von Neumann stability and dispersion analysis of a linearized version of the time-integration algorithm presented in [14, 15]. This approach is based on a predictor/multi-corrector variant of the implicit mid-point time integrator, and has the appealing property of conserving mass, momentum and total energy in the nonlinear setting, without staggering *in time* the thermodynamic variables with respect to the kinematic variables. The algorithm exactly corresponds to the staggered (in space) finite difference formulations of [2, 4] in the case of one spatial dimension and periodic boundary conditions.

Recently, the authors have discovered that the proposed algorithm *does not* yield stable solutions in the case of an odd number of iterations, and the present work is a documentation of the detailed analysis that followed these initial observations. We would also like to mention the very recent, and very interesting stability analysis [3] for the staggered scheme proposed in [4] over a two-dimensional, uniform, periodic grid. The analysis in [3] is limited to the case of the implicit mid-point algorithm and the scheme corresponding to only one predictor and one corrector passes, for the case of a purely acoustic system, with no viscosity. Our work is instead focussed on exploring the peculiar behavior of the even and odd iterations of the predictor/multi-corrector, including the effects of viscosity, and it is in agreement with the specific cases discussed in [3].

The rest of the exposition is organized as follows: Section 2 is devoted to presenting the equations of Lagrangian hydrodynamics, deriving an appropriate and representative linearization. In Section 3, a discrete system of equations is obtained in the case of one dimension and periodic boundary conditions. By means of the Discrete Fourier Transform, the von Neumann stability analysis is applied in Section 4 to the system of discrete equations. Section 5 is devoted to the analysis of the purely acoustic system of equations. In Section 6 the analysis is restricted to the highest wave numbers, with the purpose of deriving a simple stability bound for the time step in practical computations. In Section 7 the effect of viscosity on the stability of all discrete modes is also accounted for. A number of one-dimensional compressible flow computations are presented in Section 8, to confirm the theoretical findings also in the nonlinear case, for an ideal gas. A summary is presented in Section 9.

☆This research was partially funded by the DOE NNSA Advanced Scientific Computing Program and the Computer Science Research Institute at Sandia National Laboratories. Sandia is a multiprogram laboratory operated by Sandia Corporation, a Lockheed Martin Company, for the United States Department of Energy under contract DEAC04-94-AL85000.

*Corresponding author

Email addresses: gscovaz@sandia.gov (G. Scovazzi)

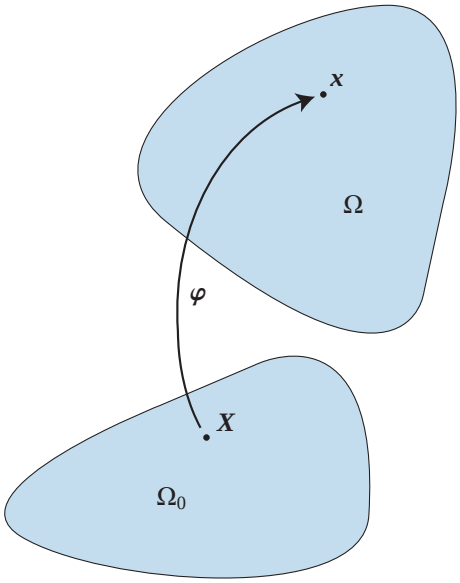

Figure 1: Sketch of the Lagrangian map $\boldsymbol{\varphi}$.

2. A simplified Lagrangian hydrodynamics system

In order to apply the von Neumann stability analysis to the system of equations of Lagrangian shock hydrodynamics, a linearization procedure is necessary. To this goal, we briefly summarize the system of Lagrangian equations for a compressible fluid in which heat fluxes, heat sources, and body forces are absent. Let Ω_0 and Ω be open sets in $\mathbb{R}^{n_d}$ (where n_d is the number of spatial dimensions). The *deformation*

$$\boldsymbol{\varphi} : \Omega_0 \rightarrow \Omega = \boldsymbol{\varphi}(\Omega_0) \,, \tag{1}$$

$$\boldsymbol{X} \mapsto \boldsymbol{x} = \boldsymbol{\varphi}(\boldsymbol{X}, t) \,, \quad \forall \boldsymbol{X} \in \Omega_0, \; t \geq 0 \,, \tag{2}$$

maps the material coordinate $\boldsymbol{X}$, representing the initial position of an infinitesimal material particle of the body, to $\boldsymbol{x}$, the position of that particle in the current configuration (see Fig. 1). Ω_0 is the domain occupied by the body in its initial configuration, with boundary Γ_0. $\boldsymbol{\varphi}$ maps Ω_0 to Ω, the domain occupied by the body in its current configuration. The *deformation gradient* and *deformation Jacobian determinant* can be defined as

$$\boldsymbol{F} = \nabla_x \boldsymbol{\varphi} \,, \tag{3}$$

$$J = \det(\boldsymbol{F}) \,, \tag{4}$$

where ∇_x is the gradient in the original configuration. In the domain Ω, the equations for the displacement update and conservation of mass, momentum, and energy read:

$$\dot{\boldsymbol{u}} = \boldsymbol{v} \,, \tag{5}$$

$$\rho J = \rho_0 \,, \tag{6}$$

$$0 = \rho \dot{\boldsymbol{v}} + \nabla_x p \,, \tag{7}$$

$$0 = \rho \dot{\epsilon} + p \nabla_x \cdot \boldsymbol{v} \,. \tag{8}$$

Here, ∇_x and $\nabla_x \cdot$ are the current configuration gradient and divergence operators, and $\dot{(\cdot)}$ indicates the material, or Lagrangian, time derivative. $\boldsymbol{u} = \boldsymbol{x} - \boldsymbol{X}$ is the displacement vector, ρ_0 is the reference (initial) density, ρ is the (current) density, $\boldsymbol{v}$ is the velocity, and p is the pressure, assumed to abide an equation of state of the type $p = \hat{p}(\rho, \epsilon)$, with ϵ the internal energy per unit mass.

In [13, 15], it was shown that the shock hydrodynamics equations can be reduced to the system form of a nonlinear wave equation. Namely, (6), (7), (8) and the equation of state yield

$$0 = \rho \dot{\boldsymbol{v}} + \nabla_x p \ , \tag{9}$$

$$0 = \dot{p} + \rho c_s^2 \nabla_x \cdot \boldsymbol{v} \ , \tag{10}$$

where c_s is the speed of sound in the medium. In the Lagrangian setting, the displacement and mass conservation equations (5)-(6) are associated with a standing (in Lagrangian coordinates) entropy wave, governing the motion of contact discontinuities. The incorporation of these equations in the analysis that follows is not essential, as the stability bounds for the systems of equations under consideration are dominated by the acoustic characteristics associated with equations (9) and (10).

Therefore, we will restrict our analysis to the system of equations (9) and (10), which can be easily linearized adopting the small strain approximation (i.e., $\nabla_x \approx \nabla_X$, the motion of the mesh is neglected), and assuming negligible time and space variations of density and speed of sound. In order to achieve insightful results, we will consider a simple one-dimensional flow with periodic boundary conditions. The reader will appreciate in what follows that the derivations are quite involved, and that these assumptions are essential to obtain meaningful results.

3. One-dimensional linearized variational formulation

We consider a weak formulation of the one-dimensional linearized equations of Lagrangian shock hydrodynamics, augmented by a shock capturing artificial viscosity operator [15]. Namely, denoting by $\mathbb{T}$ the unit periodic torus along the real line $\mathbb{R}$, we have, for every piece-wise linear (continuous) shape function ψ and every piece-wise constant (discontinuous) shape function ϕ,

$$0 = \int_{\mathbb{T}} \psi \, \dot{V} - \int_{\mathbb{T}} \psi_{,X} \, P + \int_{\mathbb{T}} \psi_{,X} \, \nu \, V_{,X} \ , \tag{11}$$

$$0 = \int_{\mathbb{T}} \phi \, \dot{P} + \int_{\mathbb{T}} \phi \, c_s^2 \, V_{,X} \ , \tag{12}$$

where, for the sake of simplicity, we have denoted $V = \rho v$ (recall $\rho = $ const.) and $P = p$. Using the same predictor/multi-corrector strategy adopted in [16], the discretization in time of (11)-(12) yields:

$$\begin{aligned} 0 = & \int_{\mathbb{T}} \psi \left(V_{n+1}^{(i+1)} - V_n \right) - \Delta t \int_{\mathbb{T}} \psi_{,X} \, P_{n+1/2}^{(i)} \\ & + \Delta t \int_{\mathbb{T}} \psi_{,X} \, \nu \, (V_{,X})_{n+1/2}^{(i)} \ , \end{aligned} \tag{13}$$

$$0 = \int_{\mathbb{T}} \phi \left(P_{n+1}^{(i+1)} - P_n \right) + \Delta t \int_{\mathbb{T}} \phi \, c_s^2 \, (V_{,X})_{n+1/2}^{(i+1)} \ , \tag{14}$$

where $(\cdot)^{(i)}$ and $(\cdot)^{(i+1)}$ are used to denote quantities computed with the predictor/corrector iterates (i) and $(i+1)$, respectively, and the subscripts n, $n+1$, and $n+1/2$ are used to indicate quantities at time t_n, $t_n + 1$, and $t_{n+1/2} = (t_n + t_{n+1})/2$.

Remark1. Observe that the latest available velocity iterate is used in the computation of the second term of (14), as in [2, 4, 14, 15], with the purpose of conserving total energy in the nonlinear setting. We adopt this time discretization to keep the analysis as close as possible to the algorithm effectively used in the computations in [2, 4, 14, 15], and we refer to this method as the *conservative* time integrator.

We assume a uniform, equispaced subdivision of the torus $\mathbb{T}$ into finite elements of measure h. The velocities are approximated by piece-wise linear functions with degrees-of-freedom collocated at the nodes of the discretization, while the pressures are approximated by piece-wise constants, with degrees-of-freedom collocated at the barycenters

of the elements (staggered spatial discretization). In addition to the previous assumptions, mass lumping is adopted in the momentum equation, yielding the following finite difference equations:

$$\begin{aligned} 0 =& V_{j,n+1}^{(i+1)} - V_{j,n} + \frac{\sigma}{2c_s}\left(P_{j+1/2,n+1}^{(i)} + P_{j+1/2,n} - P_{j-1/2,n+1}^{(i)} - P_{j-1/2,n}\right) \\ &+ \frac{\kappa}{2}\left(-V_{j+1,n+1}^{(i)} - V_{j+1,n} + 2V_{j,n+1}^{(i)} + 2V_{j,n} - V_{j-1,n+1}^{(i)} - V_{j-1,n}\right) , \end{aligned} \tag{15}$$

$$0 = P_{j+1/2,n+1}^{(i+1)} - P_{j+1/2,n} + \frac{c_s\sigma}{2}\left(V_{j+1,n+1}^{(i+1)} + V_{j+1,n} - V_{j-1,n+1}^{(i+1)} - V_{j-1,n}\right) , \tag{16}$$

where $\sigma = \frac{c_s \Delta t}{h}$ is the acoustic Courant number, $\kappa = \frac{\nu \Delta t}{h^2}$, and j is the node index.

Remark2. In the simple one-dimensional, periodic case, equations (15)–(16) exactly coincide with the one-dimensional version of the finite difference schemes detailed in [2, 4].

4. Von Neumann stability analysis

As customary in the von Neumann stability analysis (see [11, 17] for details), because the boundary conditions are periodic, we can expand the solution degrees-of-freedom as a finite, linear combination of complex exponentials with complex coefficients. This eventually amounts to applying a Discrete Fourier Transform (DFT) operator to the discrete equations (15)–(16). In particular, we have:

$$V_{j,n}^{(i)} = \sum_{k=-N/2+1}^{N/2} \hat{V}_{k,n}^{(i)} e^{\mathrm{i}\beta_k j} , \tag{17}$$

$$P_{j+1/2,n}^{(i)} = \sum_{k=-N/2+1}^{N/2} \hat{P}_{k,n}^{(i)} e^{\mathrm{i}\beta_k (j+1/2)} , \tag{18}$$

where $\mathrm{i} = \sqrt{-1}$, and $\hat{V}_{k,n}^{(i)}$ is the Fourier coefficient associated with the kth harmonic, time step n and iterate (i). Note that N is the number of elements (a multiple of 2), and $\beta_k = \frac{2\pi h k}{|\mathbb{T}|} = \frac{2\pi k}{N}$ is an angularly scaled version of the integer wave number k (with $|\mathbb{T}| = \mathrm{meas}(\mathbb{T}) = Nh = 1$ the measure of the torus). Complex exponentials associated to different wave numbers satisfy a discrete orthogonality property:

$$\sum_{m=-N/2}^{N/2-1} e^{\mathrm{i}\beta_k m} e^{\mathrm{i}\beta_q m} = \delta_{kq} , \quad \text{for } -N/2 \le k, q \le N/2 , \tag{19}$$

with δ_{kq} the Kronecker delta tensor ($\delta_{kq} = 1$ if $k = q$, and $\delta_{kq} = 0$ if $k \neq q$). We then substitute (17)-(18) into (15)-(16) multiplied by $e^{\mathrm{i}\beta_{k_1} j}$ and $e^{\mathrm{i}\beta_{k_2}(j+1/2)}$, respectively, and we sum over j. We multiply (16) by $e^{\mathrm{i}\beta_{k_2}(j+1/2)}$ instead of $e^{\mathrm{i}\beta_{k_2} j}$, in order to simplify the algebra, as the pressure variable is staggered in space with respect to the momentum equation.

Due to the orthogonality property (19), and the linearity of the system of equations (15)-(16), it is easy to verify that the previous steps lead to N pairs of equations, coupling the dynamics of the kth pressure and velocity modes, with $-N/2 + 1 \le k \le N/2$. Namely:

$$(\boldsymbol{I} + \boldsymbol{A}_0)\hat{\boldsymbol{Z}}_{k,n+1}^{(i+1)} = \boldsymbol{A}_1 \hat{\boldsymbol{Z}}_{k,n+1}^{(i)} + (\boldsymbol{I} + \boldsymbol{A}_2)\hat{\boldsymbol{Z}}_{k,n} , \tag{20}$$

where

$$\hat{\boldsymbol{Z}}_{k,n}^{(i)} = \begin{Bmatrix} \hat{V}_{k,n}^{(i)} \\ \hat{P}_{k,n}^{(i)} \end{Bmatrix} \tag{21}$$

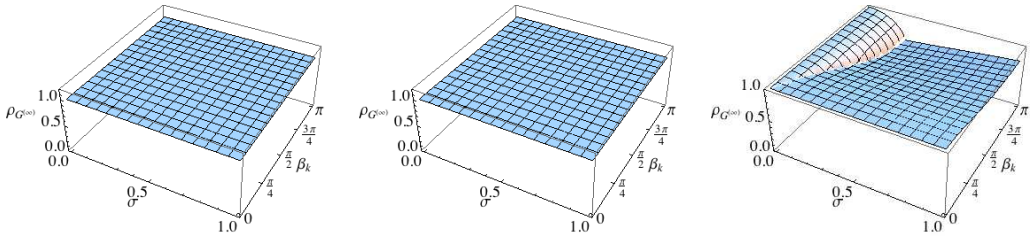

(a) Implicit. $\kappa = 0$. (b) Implicit. $\kappa = 0$. (c) Implicit. $\kappa = 1/4$.

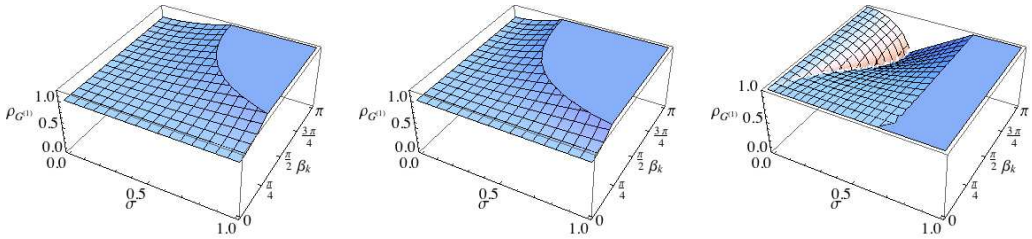

(d) 1st iterate. $\kappa = 0$. (C) (e) 1st iterate. $\kappa = 0$. (L) (f) 1st iterate. $\kappa = 1/4$. (C)

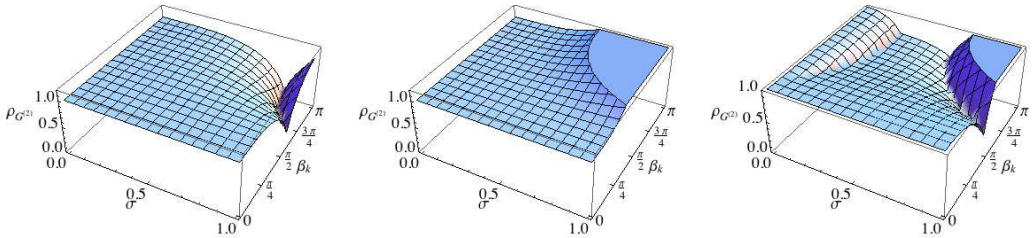

(g) 2nd iterate. $\kappa = 0$. (C) (h) 2nd iterate. $\kappa = 0$. (L) (i) 2nd iterate. $\kappa = 1/4$. (C)

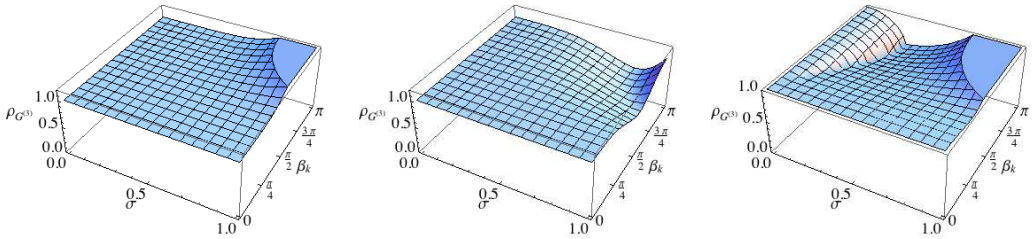

(j) 3rd iterate. $\kappa = 0$. (C) (k) 3rd iterate. $\kappa = 0$. (L) (l) 3rd iterate. $\kappa = 1/4$. (C)

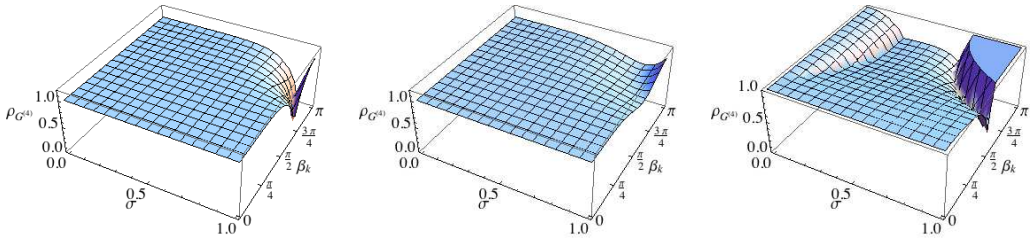

(m) 4th iterate. $\kappa = 0$. (C) (n) 4th iterate. $\kappa = 0$. (L) (o) 4th iterate. $\kappa = 1/4$. (C)

Figure 2: Elevation plots of the spectral radii $\rho_{\mathbf{G}^{(i)}}(\sigma, \beta_k)$ for $\kappa = 0$, $\kappa = 1/4$, and various iterates of the predictor/multi-corrector algorithm. In the top row, the implicit mid-point time integrator detailed in (39). In the subsequent rows, in ascending order, the iterates from one to four. Note that in Figures 2(a), 2(b), 2(d), 2(e), 2(g), 2(h), 2(j), 2(k), 2(m), and 2(n) the vertical range is $[0, 1.2]$, while in Figures 2(c), 2(f), 2(i), 2(l), 2(o) the vertical range is $[0, 1]$. Also note that Figures 2(a) and 2(b) are identical.

is the kth velocity/pressure modal pair, relative to the nth time step and the ith iterate, and

$$\boldsymbol{I} = \begin{bmatrix} 1 & 0 \\ 0 & 1 \end{bmatrix}, \tag{22}$$

$$\boldsymbol{A}_0 = \begin{bmatrix} 0 & 0 \\ \mathrm{i}\frac{c_s}{2}\sigma \sin\left(\frac{\beta_k}{2}\right) & 0 \end{bmatrix}, \tag{23}$$

$$\boldsymbol{A}_1 = \begin{bmatrix} \kappa(\cos(\beta_k) - 1) & -\mathrm{i}\frac{1}{2c_s}\sigma \sin\left(\frac{\beta_k}{2}\right) \\ 0 & 0 \end{bmatrix}, \tag{24}$$

$$\boldsymbol{A}_2 = \begin{bmatrix} \kappa(\cos(\beta_k) - 1) & -\mathrm{i}\frac{1}{2c_s}\sigma \sin\left(\frac{\beta_k}{2}\right) \\ -\mathrm{i}\frac{c_s}{2}\sigma \sin\left(\frac{\beta_k}{2}\right) & 0 \end{bmatrix}. \tag{25}$$

It is also very important to observe that because the degrees-of-freedom "signal" has real values, the discrete Fourier coefficients must satisfy the complex conjugacy property

$$\hat{\boldsymbol{Z}}^{(i)}_{-k,n} = \left(\hat{\boldsymbol{Z}}^{(i)}_{k,n}\right)^* , \quad \text{for } 0 \le k \le N/2 - 1 , \tag{26}$$

where $\hat{\boldsymbol{W}}^*$ indicates the complex conjugate of $\hat{\boldsymbol{W}}$ (componentwise). For the same reason, the following condition on the often called "odd ball" mode holds:

$$\hat{\boldsymbol{Z}}^{(i)}_{N/2,n} = \boldsymbol{0} . \tag{27}$$

Because complex conjugates have the same absolute value and opposite phase, it is sufficient to limit the study of the amplification factors for the modes of the discrete system to the range $0 \le k < N/2$, that is, $0 \le \beta_k < \pi$. In the discussion that follows, it will also be important to consider a variation of the time-integration algorithm, in which the velocity iterate $V^{(i+1)}$ in (16) is replaced by the previous iterate $V^{(i)}$. This method will be referred to as the *lagged* approach. In this case, equation (16) becomes

$$0 = P^{(i+1)}_{j+1/2,n+1} - P_{j+1/2,n} + \frac{c_s\sigma}{2}\left(V^{(i)}_{j+1,n+1} + V_{j+1,n} - V^{(i)}_{j-1,n+1} - V_{j-1,n}\right) , \tag{28}$$

and, consequently, $\boldsymbol{A}_0$ and $\boldsymbol{A}_1$ need to be modified as:

$$\boldsymbol{A}_0 = \boldsymbol{0} , \tag{29}$$

$$\boldsymbol{A}_1 = \boldsymbol{A}_2 . \tag{30}$$

This approach yields a more straightforward time integrator for the linearized equations, which does not extend, however, to a conservative scheme in the nonlinear case.

The vector equation (20) is a recurrence relationship between the predictor/multi-corrector iterates of the proposed time-integration approach. Set

$$\boldsymbol{B}_0 = (\boldsymbol{I} + \boldsymbol{A}_0)^{-1}(\boldsymbol{I} + \boldsymbol{A}_2) , \tag{31}$$

$$\boldsymbol{B}_1 = (\boldsymbol{I} + \boldsymbol{A}_0)^{-1}\boldsymbol{A}_1 , \tag{32}$$

and recall that the first guess for the new iterate at time t_{n+1} is the solution at time t_n, namely $\hat{\boldsymbol{Z}}^{(0)}_{k,n+1} = \hat{\boldsymbol{Z}}_{k,n}$. Then, we can derive explicit recurrence formulas for the computation of $\hat{\boldsymbol{Z}}^{(i+1)}_{k,n+1}$ in terms of $\hat{\boldsymbol{Z}}_{k,n}$:

$$\begin{aligned} \hat{\boldsymbol{Z}}^{(1)}_{k,n+1} &= \boldsymbol{B}_1\hat{\boldsymbol{Z}}^{(0)}_{k,n+1} + \boldsymbol{B}_0\hat{\boldsymbol{Z}}_{k,n} \\ &= (\boldsymbol{B}_0 + \boldsymbol{B}_1)\hat{\boldsymbol{Z}}_{k,n} \\ &= \boldsymbol{G}^{(1)}\hat{\boldsymbol{Z}}_{k,n} , \end{aligned} \tag{33}$$

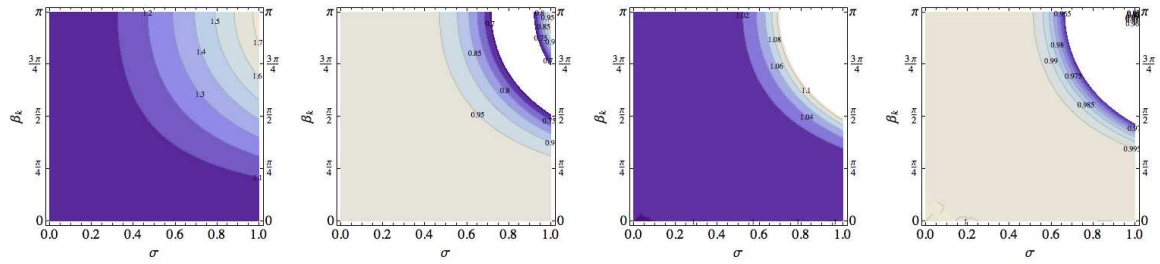

(a) 1st iterate (C) (b) 2nd iterate (C) (c) 3rd iterate (C) (d) 4th iterate (C)

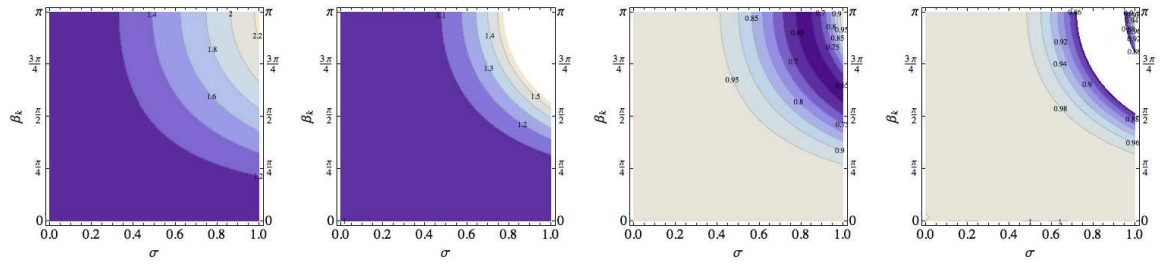

(e) 1st iterate (L) (f) 2nd iterate (L) (g) 3rd iterate (L) (h) 4th iterate (L)

Figure 3: Contour plots of the spectral radii of various iterates of the predictor/multi-corrector algorithm for $\kappa = 0$. Figures 3(a), 3(b), 3(c), and 3(d): Conservative scheme (C). Figures 3(e), 3(f), 3(g), and 3(h): Lagged scheme (L).

$$\begin{aligned}\hat{\boldsymbol{Z}}^{(2)}_{k,n+1} &= \boldsymbol{B}_1\hat{\boldsymbol{Z}}^{(1)}_{k,n+1} + \boldsymbol{B}_0\hat{\boldsymbol{Z}}_{k,n} \\ &= \left(\boldsymbol{B}_1\boldsymbol{G}^{(1)} + \boldsymbol{B}_0\right)\hat{\boldsymbol{Z}}_{k,n} \\ &= \boldsymbol{G}^{(2)}\hat{\boldsymbol{Z}}_{k,n}\ , \end{aligned} \tag{34}$$

$$\begin{aligned}\hat{\boldsymbol{Z}}^{(3)}_{k,n+1} &= \boldsymbol{B}_1\hat{\boldsymbol{Z}}^{(2)}_{k,n+1} + \boldsymbol{B}_0\hat{\boldsymbol{Z}}_{k,n} \\ &= \left(\boldsymbol{B}_1\boldsymbol{G}^{(2)} + \boldsymbol{B}_0\right)\hat{\boldsymbol{Z}}_{k,n} \\ &= \boldsymbol{G}^{(3)}\hat{\boldsymbol{Z}}_{k,n}\ , \end{aligned} \tag{35}$$

$$\begin{aligned}\hat{\boldsymbol{Z}}^{(4)}_{k,n+1} &= \boldsymbol{B}_1\hat{\boldsymbol{Z}}^{(3)}_{k,n+1} + \boldsymbol{B}_0\hat{\boldsymbol{Z}}_{k,n} \\ &= \left(\boldsymbol{B}_1\boldsymbol{G}^{(3)} + \boldsymbol{B}_0\right)\hat{\boldsymbol{Z}}_{k,n} \\ &= \boldsymbol{G}^{(4)}\hat{\boldsymbol{Z}}_{k,n}\ , \end{aligned} \tag{36}$$

$$\hat{\boldsymbol{Z}}^{(5)}_{k,n+1} = \ldots\ , \tag{37}$$

In the limit for an infinite number of iterations, we obtain the amplification matrix for the original implicit mid-point algorithm from which the predictor/corrector time integrator is derived:

$$(\boldsymbol{I} + \boldsymbol{A}_0)\hat{\boldsymbol{Z}}^{(\infty)}_{k,n+1} = \boldsymbol{A}_1\hat{\boldsymbol{Z}}^{(\infty)}_{k,n+1} + (\boldsymbol{I} + \boldsymbol{A}_2)\hat{\boldsymbol{Z}}_{k,n}\ , \tag{38}$$

that is, removing the superscript (∞) from $\hat{\boldsymbol{Z}}^{(\infty)}_{k,n+1}$, and rearranging terms,

$$\begin{aligned}\hat{\boldsymbol{Z}}_{k,n+1} &= (\boldsymbol{I} + \boldsymbol{A}_0 - \boldsymbol{A}_1)^{-1}(\boldsymbol{I} + \boldsymbol{A}_2)\ \hat{\boldsymbol{Z}}_{k,n} \\ &= \boldsymbol{G}^{(\infty)}\hat{\boldsymbol{Z}}_{k,n}\ . \end{aligned} \tag{39}$$

Remark3. The predictor/multi-corrector method can therefore be interpreted as a fixed-point iterative process, converging to the solution of the implicit method (39). In particular, the conservative scheme has the nature of a Gauss-Seidel iteration, as the matrix $\boldsymbol{I} + \boldsymbol{A}_0$ is lower diagonal, while the lagged scheme resembles a Jacobi iteration, since in this case $\boldsymbol{A}_0 = \boldsymbol{0}$.

Remark4. Convergence of the fixed-point iteration is ensured if $\|\boldsymbol{B}_1\| < 1$ (sufficient condition). It will be subsequently shown that this condition is equivalent to the temporal stability condition.

It is possible to evaluate the stability properties of the proposed predictor/multi-corrector algorithm, by evaluating how $\boldsymbol{G}^{(i)}$ evolves in time an initial condition. In particular, if

$$\|\boldsymbol{G}^{(i)}\| = \max_{\boldsymbol{s}\in\mathbb{R}^2\setminus\boldsymbol{0}} \frac{\|\boldsymbol{G}^{(i)}\boldsymbol{s}\|}{\|\boldsymbol{s}\|} \leq 1 \tag{40}$$

then stability of the numerical discretization is ensured. Defining the spectral radius as

$$\rho(\boldsymbol{G}^{(i)}) = \max\{|\lambda(\boldsymbol{G}^{(i)})|\} \leq \|\boldsymbol{G}^{(i)}\| \,, \tag{41}$$

where $\lambda(\boldsymbol{G}^{(i)})$ is a (generally complex) eigenvalue of $\boldsymbol{G}^{(i)}$, we can recast condition (40) as (see [7])

$$\rho(\boldsymbol{G}^{(i)}) < 1 \Rightarrow \text{ stability} \,, \tag{42}$$

$$\rho(\boldsymbol{G}^{(i)}) > 1 \Rightarrow \text{ instability} \,. \tag{43}$$

These conditions are consequence of a well-known theorem in matrix analysis:

Theorem 1 (cf. [8], p. 298). *Let $\boldsymbol{A} \in \mathbb{C}^{m\times m}$, where $\mathbb{C}$ is the complex field. Then:* $\lim_{n\to\infty} \boldsymbol{A}^n = \boldsymbol{0}$ *if and only if* $\rho(\boldsymbol{A}) < 1$.

Hence, if $\rho(\boldsymbol{G}^{(i)}) < 1$, Theorem 1 directly implies stability. If $\rho(\boldsymbol{G}^{(i)}) > 1$, one can consider, as initial condition vector $\hat{\boldsymbol{Z}}_0$, the eigenvector relative to an eigenvalue λ_0 with $|\lambda_0| > 1$. Using the properties of vector norms, it is easy to see that $\lim_{n\to\infty} \|\hat{\boldsymbol{Z}}_n\| = \lim_{n\to\infty} \|(\boldsymbol{G}^{(i)})^n \hat{\boldsymbol{Z}}_0\| = \lim_{n\to\infty} |\lambda_0|^n \|\hat{\boldsymbol{Z}}_0\| = \infty$, and we have instability. The case that our analysis covers less precisely is the case when $\rho(\boldsymbol{G}^{(i)}) = 1$. Recalling that (see [8], p. 299)

$$\rho(\boldsymbol{G}^{(i)}) = \lim_{n\to\infty} \|(\boldsymbol{G}^{(i)})^n\|^{1/n} \,, \tag{44}$$

it is easy to realize that the case $\rho(\boldsymbol{G}^{(i)}) = 1$ admits linear growth in the solution (i.e., $\|(\boldsymbol{G}^{(i)})^n\| = O(n)$). However, the analysis that follows (see, e.g., Figure 2) shows that $\rho(\boldsymbol{G}^{(i)}) = 1$ occurs in three special cases :

1. $\sigma = 0 \Leftrightarrow \Delta t = 0$, a trivial case corresponding of no time evolution.
2. $\beta_k = 0$, corresponding to the evolution in time of a constant mode. In this case, it is not necessary to resort to the von Neumann analysis, to prove that the entire class of algorithms under consideration *stably* preserves constant solutions in time.
3. The time-step stability limit, as a limit case of the condition $\rho(\boldsymbol{G}^{(i)}) < 1$. This case is not so important in practical (nonlinear) computations, since it is usually not safe to run computations exactly at the stability limit.

Notice also that a complex eigenvalue of $\boldsymbol{G}^{(i)}$ can be expressed as:

$$\lambda(\boldsymbol{G}^{(i)}) = |\lambda(\boldsymbol{G}^{(i)})| e^{\mathrm{i}\bar{\omega}\Delta t} \,, \tag{45}$$

where $\bar{\omega}\Delta t = \arg(\lambda(\boldsymbol{G}^{(i)}))$, and $\bar{\omega} \in \mathbb{R}$ is the phase. This decomposition will be important for the study of the dispersion properties of the proposed time integration approach. An alternative expression for (45) is

$$\lambda(\boldsymbol{G}^{(i)}) = e^{(-\bar{\xi}+\mathrm{i}\bar{\omega})\Delta t} \,, \tag{46}$$

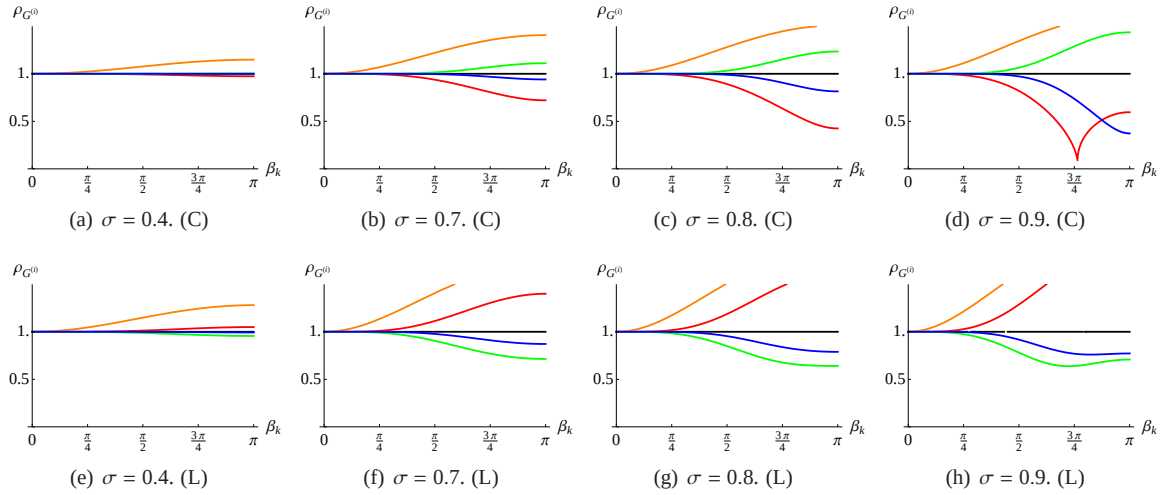

(a) $\sigma = 0.4$. (C) (b) $\sigma = 0.7$. (C) (c) $\sigma = 0.8$. (C) (d) $\sigma = 0.9$. (C)

(e) $\sigma = 0.4$. (L) (f) $\sigma = 0.7$. (L) (g) $\sigma = 0.8$. (L) (h) $\sigma = 0.9$. (L)

Figure 4: Spectral radii for the predictor/multi-corrector algorithm in the case $\kappa = 0$, for various values of the acoustic Courant number σ. Figures 4(a)–4(d): Conservative scheme. Figures 4(e)–4(h): Lagged scheme. Black: Implicit time integrator. Orange, red, green and blue are used for the first, second, third, and fourth iterate, respectively.

where

$$|\lambda(\boldsymbol{G}^{(i)})| = e^{-\bar{\xi}\Delta t}\,, \qquad \text{or,} \quad \bar{\xi} = -\frac{\log(|\lambda(\boldsymbol{G}^{(i)})|)}{\Delta t}\,. \tag{47}$$

By performing a Taylor expansion of $\bar{\xi}$ and $\bar{\omega}$ in the limit of vanishing time step Δt and mesh size h, it is possible to recover the truncation error and the formal order of accuracy of the various iterates of the method.

Due to the complexity of the algebra involved, we are not including the calculations and explicit expressions of the eigenvalues of the $\boldsymbol{G}^{(i)}$ matrices in the general case. We will present the fundamental results by appropriate plots in Section 5 and Section 7. All algebraic symbolic manipulations were performed using the MATHEMATICA® ™ software [1, 18].

5. The case of vanishing viscosity

In shock hydrodynamics computations, the artificial viscosity is usually present only in shock layers, and absent in expansion regions. Therefore, it is very important to study the proposed time integrator in the limit of a vanishing viscosity, as most of the flow domain is subject to this condition.

5.1. Amplification factor

Figure 2 shows the spectral radii of the matrices $\boldsymbol{G}^{(i)}$ for $i = 1, 2, 3, 4$ and $i \to \infty$ (implicit limit), for the conservative and lagged algorithms in the case $\kappa = 0$, and also for the conservative algorithm when $\kappa = 1/4$. For the time being, we focus on the plots relative to $\kappa = 0$.

First, note that the implicit algorithm detailed in (39) is neutrally stable (Fig. 2(a) and 2(b)), as the spectral radius of the corresponding amplification matrix is equal to unity over the entire plane $[\sigma, \beta]$. The first and third iterates of the conservative algorithm (C) are *unconditionally unstable*, while the second and fourth iterates are conditionally stable, as shown in Figures 2(g) and 2(m). This phenomenon, somewhat surprising, can be explained by realizing that the spectral radii for the predictor/multi-corrrector scheme exhibit a *non-monotonic* convergence to unity as $(i) \to \infty$. Observe that the situation for the lagged algorithm is somewhat different, since the first two iterates are unconditionally unstable (Fig. 2(e) and 2(h)), but the subsequent third and fourth iterates regain conditional stability in the range $\sigma \in [0, 1]$ (Fig. 2(k) and 2(n)). This fact can easily be observed in the contour plots of the spectral radii presented in Figure 3, and perhaps even more clearly in the sections at various values of σ presented in Figure 4.

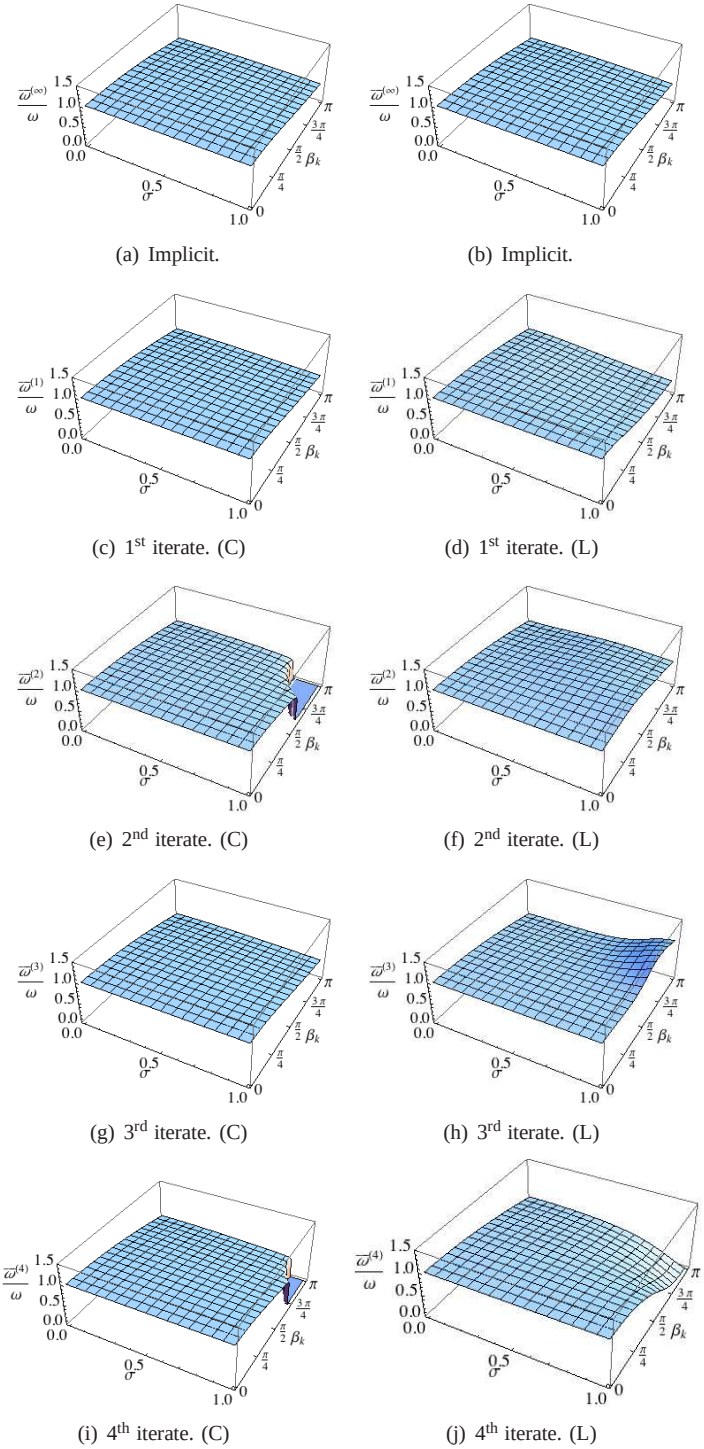

(a) Implicit. (b) Implicit.

(c) 1st iterate. (C) (d) 1st iterate. (L)

(e) 2nd iterate. (C) (f) 2nd iterate. (L)

(g) 3rd iterate. (C) (h) 3rd iterate. (L)

(i) 4th iterate. (C) (j) 4th iterate. (L)

Figure 5: Elevation plots of the dispersion ratio $\bar{\omega}/\omega$, for $\kappa = 0$, and various iterates of the predictor/multi-corrector algorithm. In the top row, the implicit mid-point time integrator detailed in (39). In the subsequent rows, in ascending order, the iterates from one to four. Figures 5(a), 5(c), 5(e), 5(g), 5(i) refer to the conservative algorithm (C), Figures 5(b), 5(d), 5(f), 5(h), 5(j) refer to the lagged algorithm (L). Also note that Figures 5(a) and 5(b) are identical.

Also note in Figure 4(d) that the second iterate, indicated by a red line, shows the insurgence of a bifurcation (a kink in the red curve, near $\beta_k = 3\pi/4$). Past the bifurcation point, the eigenvalues of the amplification matrix cease to be complex conjugate and become real, as also evident in Figure 7(d), by the absence of a phase in the eigenvalues. This is not a desirable property in wave propagation problems, where one would expect the discretized equations to behave as a system of harmonic oscillators. Past the bifurcation point, the discrete solutions become real exponentials in time, and cause an incorrect representation of the structure of the original system of partial differential equations. The lagged algorithm does not show this behavior.

5.2. Dispersion error

When no viscosity is present, it is very insightful to evaluate the extent of the dispersion error in computations. This can be done by observing that the classical dispersion relationship for a linear wave is given by $\omega = 2\pi k c_s/|\mathbb{T}|$. Recalling that $\mathbb{T} = hN$, it is easy to derive that

$$\omega \Delta t = \sigma \beta_k \ . \tag{48}$$

A typical measure of the dispersion error is given by the ratio

$$\frac{\bar{\omega}}{\omega} = \frac{\arg(\lambda(\sigma, \beta_k))}{\sigma \beta_k} \ . \tag{49}$$

Figure 5 shows elevation plots of the ratio $\bar{\omega}/\omega$. It is noticeable in Figures 5(e) and 5(i) that bifurcation takes place for values of $[\sigma, \beta_k]$ in the neighborhood of $[1, \pi]$, for the second and forth iterate of the conservative algorithm, respectively. As already mentioned, this behavior is not present for the lagged scheme.

Contour plots of the dispersion ratio are presented in Figure 6. The black thick lines indicate the loci where the dispersion ratio equals unity, that is, optimal behavior (no phase error).

Comparing the various results in Figure 7, notice the good behavior of the conservative approach in retaining the dispersion properties of the corresponding implicit method, at least until a bifurcation arises for the second iterate (see Figs. 7(a), 7(b), 7(c), and 7(d)). This is not the case for the lagged scheme, for which all the iterates have quite different phase characterization with respect to the implicit method (Figs. 7(e), 7(f), 7(g), and 7(h)).

5.3. Low wave number limit and truncation error

A Taylor expansion of the amplification factor ρ and dispersion ratio $\bar{\omega}/\omega$ in a right neighborhood of $\beta_k = 0$ can more clearly quantify the previous conclusions on the nature of the proposed conservative algorithm.

$$\rho(\boldsymbol{G}^{(1)}) = 1 + \frac{\sigma^2 \beta_k^2}{4} + O(\beta_k^3) \ , \qquad \frac{\bar{\omega}(\boldsymbol{G}^{(1)})}{\omega} = 1 - \frac{4 + 11\sigma^2}{96} \beta_k^2 + O(\beta_k^4) \ , \tag{50}$$

$$\rho(\boldsymbol{G}^{(2)}) = 1 - \frac{\sigma^4 \beta_k^4}{16} + O(\beta_k^5) \ , \qquad \frac{\bar{\omega}(\boldsymbol{G}^{(2)})}{\omega} = 1 - \frac{2 + \sigma^2}{24} \beta_k^2 + O(\beta_k^4) \ , \tag{51}$$

$$\rho(\boldsymbol{G}^{(3)}) = 1 + \frac{\sigma^6 \beta_k^6}{64} + O(\beta_k^7) \ , \qquad \frac{\bar{\omega}(\boldsymbol{G}^{(3)})}{\omega} = 1 - \frac{2 + \sigma^2}{24} \beta_k^2 + O(\beta_k^4) \ , \tag{52}$$

$$\rho(\boldsymbol{G}^{(4)}) = 1 - \frac{\sigma^8 \beta_k^8}{256} + O(\beta_k^9) \ , \qquad \frac{\bar{\omega}(\boldsymbol{G}^{(4)})}{\omega} = 1 - \frac{2 + \sigma^2}{24} \beta_k^2 + O(\beta_k^4) \ . \tag{53}$$

Hence, it is clearly noticeable the fact that the low modes are amplified for odd iterates and damped for even iterates. The dispersion of low modes, instead, seems to maintain the same limit behavior as soon as the number of iterates is larger than one. Furthermore, a Taylor series expansion of $\bar{\xi}$ and $\bar{\omega}$ in powers of Δt and h allows to evaluate the order

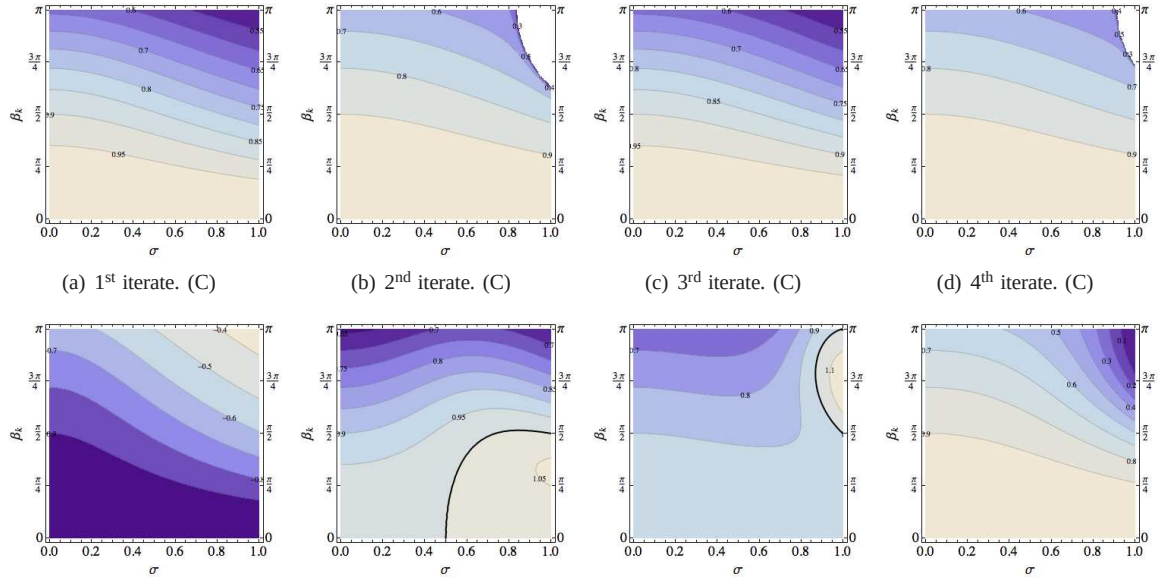

(a) 1st iterate. (C) (b) 2nd iterate. (C) (c) 3rd iterate. (C) (d) 4th iterate. (C)

(e) 1st iterate. (L) (f) 2nd iterate. (L) (g) 3rd iterate. (L) (h) 4th iterate. (L)

Figure 6: Contour plots of the ratio $\bar{\omega}/\omega$, for $\kappa = 0$, and various iterates of the predictor/multi-corrector algorithm. Figures 6(a), 6(b), 6(c), and 6(d): Conservative scheme. Figures 6(e), 6(f), 6(g), and 6(h): Lagged scheme. The black continuous line indicates the locus $\bar{\omega}/\omega = 1$.

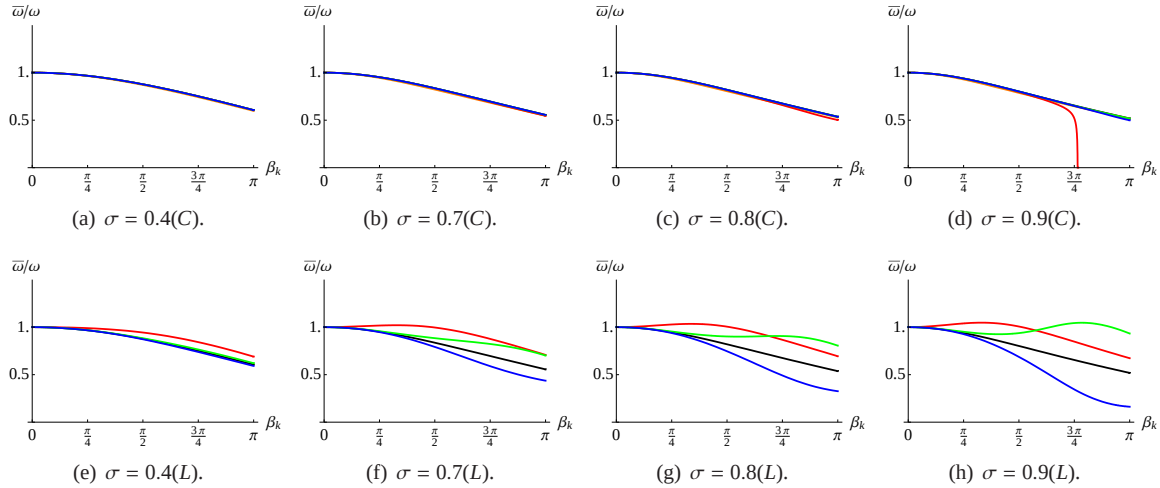

(a) $\sigma = 0.4(C)$. (b) $\sigma = 0.7(C)$. (c) $\sigma = 0.8(C)$. (d) $\sigma = 0.9(C)$.

(e) $\sigma = 0.4(L)$. (f) $\sigma = 0.7(L)$. (g) $\sigma = 0.8(L)$. (h) $\sigma = 0.9(L)$.

Figure 7: Plot of the ratio $\bar{\omega}/\omega$, for $\kappa = 0$, for various values of the acoustic Courant number σ. Figures 7(a)–7(d): Conservative scheme. Figures 7(e)–7(h): Lagged scheme. Color scheme is as follows. Black is used for the implicit version of the algorithm. Orange, red, green and blue are used for the first, second, third, and fourth iterate, respectively.

of convergence of the proposed method. We obtain:

$$\bar{\xi}(\boldsymbol{G}^{(1)}) = -\frac{1}{4}c_s^2\tilde{k}^2\Delta t + O(h^2\Delta t)\,, \tag{54}$$

$$\bar{\omega}(\boldsymbol{G}^{(1)}) = \omega - \frac{1}{24}c_s h^2\tilde{k}^3 - \frac{11}{96}c_s^3\tilde{k}^3\Delta t^2 + O(\Delta t^2 h^2)\,, \tag{55}$$

$$\bar{\xi}(\boldsymbol{G}^{(2)}) = \frac{1}{16}c_s^4\tilde{k}^4\Delta t^3 + O(h^2\Delta t^3)\,, \tag{56}$$

$$\bar{\omega}(\boldsymbol{G}^{(2)}) = \omega - \frac{1}{24}c_s h^2\tilde{k}^3 - \frac{1}{12}c_s^3\tilde{k}^3\Delta t^2 + O(\Delta t^2 h^2)\,, \tag{57}$$

$$\bar{\xi}(\boldsymbol{G}^{(3)}) = -\frac{1}{64}c_s^6\tilde{k}^6\Delta t^5 + O(h^2\Delta t^5)\,, \tag{58}$$

$$\bar{\omega}(\boldsymbol{G}^{(3)}) = \omega - \frac{1}{24}c_s h^2\tilde{k}^3 - \frac{1}{12}c_s^3\tilde{k}^3\Delta t^2 + O(\Delta t^2 h^2)\,, \tag{59}$$

$$\bar{\xi}(\boldsymbol{G}^{(4)}) = \frac{1}{256}c_s^8\tilde{k}^8\Delta t^7 + O(h^2\Delta t^7)\,, \tag{60}$$

$$\bar{\omega}(\boldsymbol{G}^{(4)}) = \omega - \frac{1}{24}c_s h^2\tilde{k}^3 - \frac{1}{12}c_s^3\tilde{k}^3\Delta t^2 + O(\Delta t^2 h^2)\,, \tag{61}$$

where $\tilde{\kappa} = 2\pi k/|\mathbb{T}|$, so that $\omega = \tilde{\kappa}c_s$. Consequently, the first, second, third and fourth iterates of the predictor/multi-corrector conservative method are first-, third-, fifth- and seventh-order accurate with respect to the dissipation error. All iterates are second-order accurate with respect to the dispersion error.

6. Stability of the highest wavembers

Before proceeding with the case in which dissipation is present, it is important to develop a preliminary analysis of stability for the highest spatial wave numbers in the discrete equations. Stability of the highest modes in the computation is a necessary *but not sufficient* condition for overall stability. However, an understanding on the high wave number dynamics can shed light on the overall behavior of the algorithm, and, most importantly, provide stable time estimates of practical use in computations.

The amplification of the highest wave number is governed by the matrices $\boldsymbol{G}^{(i)}$, when β_k is set equal to π. In this case, a number of algebraic manipulations leads to the following expressions for the eigenvalues of the matrices $\boldsymbol{G}^{(i)}$'s:

$$\lambda_{1,2}^{(1)} = 1 - \sigma^2 - 2\kappa \tag{62}$$

$$\mp\sqrt{\sigma^4 + 4\sigma^2(-1+\kappa) + 4\kappa^2}\,, \tag{63}$$

$$\lambda_{1,2}^{(2)} = 1 - 2\sigma^2 + \sigma^4 - 2\kappa + 4\sigma^2\kappa + 4\kappa^2 \tag{64}$$

$$\mp\sqrt{-1 + 2\sigma^4 + 4\kappa - 8\kappa^2 + (1 + \sigma^4 - 2\kappa + 4\kappa^2 + \sigma^2(-2+4\kappa))^2}\,, \tag{65}$$

$$\lambda_{1,2}^{(3)} = \dots\,, \tag{66}$$

where we have omitted the derivations for the third and higher iterates, since the algebraic expressions become very complex and tedious to manipulate. Let us consider the second iterate, that is the first iterate for which second-order accuracy is achieved, and analyze the stability condition $-1 \le \lambda_{1,2}^{(2)} \le 1$. Only the right bound is meaningful for stability. Setting $\lambda_{1,2}^{(2)} = 1$ yields a polynomial equation, with roots $\sigma = 0$, $\sigma = -\sqrt{1-2\kappa}$, and $\sigma = \sqrt{1-2\kappa}$. Only the last root is useful in defining a stability limit, which, taking squares, reads

$$\sigma^2 + 2\kappa - 1 \le 0\,, \qquad \text{or,} \qquad c_s^2\Delta t^2 + 2\nu\Delta t - h^2 \le 0\,. \tag{67}$$

The same condition is derived in the case of four iterations of the predictor/multi-corrector algorithm, with much more complex algebraic manipulations. Solving the quadratic equation associated with (67) yields the bounds

$$\frac{-\nu - \sqrt{\nu^2 + c_s^2 h^2}}{c_s^2} \le \Delta t \le \frac{-\nu + \sqrt{\nu^2 + c_s^2 h^2}}{c_s^2}\,. \tag{68}$$

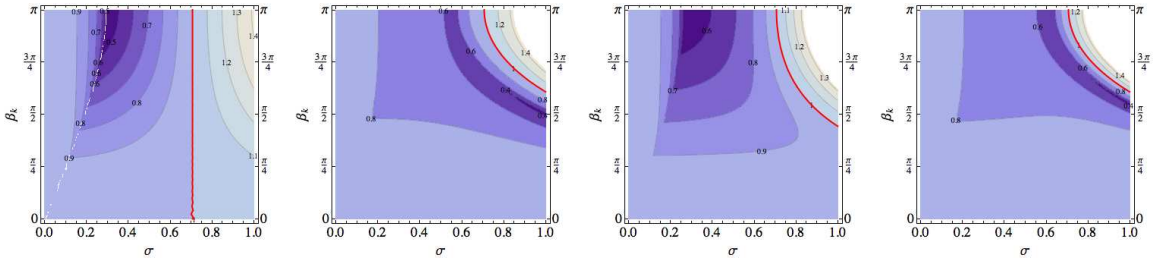

(a) 1st iterate. (b) 2nd iterate. (c) 3rd iterate. (d) 4th iterate.

Figure 8: Contour plots of the spectral radii for various predictor/multi-corrector iterates of the conservative algorithm, in the case $\kappa = 1/4$. The red continuous line correspond to the isoline for the spectral radius equal to unity.

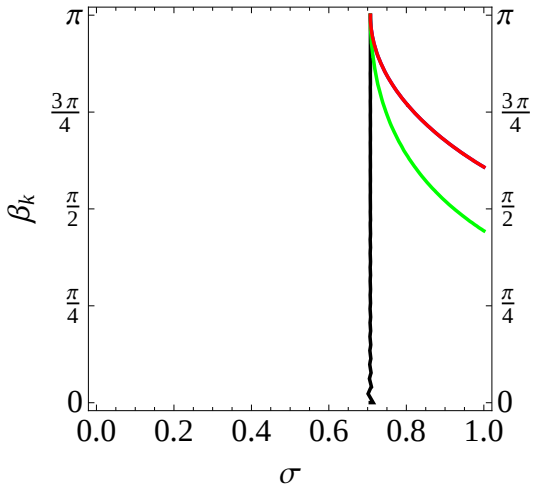

Figure 9: Contour plots of the loci of the spectral radii equal to unity, in the case $\kappa = 1/4$. The color scheme is as follows. First iterate in black, second iterate in blue, third iterate in green, fourth iterate in red. The curve relative to the second iterate is not visible as it overlaps with the one relative to the fourth iterate.

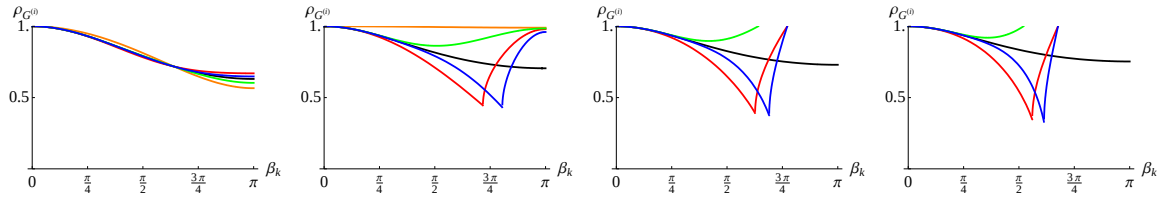

(a) $\sigma = 0.4$. (b) $\sigma = 0.7$. (c) $\sigma = 0.8$. (d) $\sigma = 0.9$.

Figure 10: Spectral radii for the predictor/multi-corrector algorithm in the case $\kappa = 1/4$, for various values of the acoustic Courant number σ, for the conservative scheme. Color scheme is as follows. Black: Implicit time integrator. Orange, red, green and blue are used for the first, second, third, and fourth iterate, respectively.

The left bound is always verified, while the right gives the stability limit. Multiplying and dividing the entire inequality by $\nu + \sqrt{\nu^2 + c_s^2 h^2}$ (always a strictly positive quantity) and simplifying the term c_s^2, we obtain

$$\Delta t \leq \frac{h^2}{\nu + \sqrt{\nu^2 + c_s^2 h^2}} \, . \tag{69}$$

Remark5. In the limit of a vanishing artificial viscosity, the acoustic Courant-Friedrichs-Levy condition is obtained, namely,

$$\Delta t \leq \frac{h}{c_s} \, , \qquad \text{or,} \qquad \sigma \leq 1 \, . \tag{70}$$

Remark6. In the limit of a vanishing speed of sound (condition very often encountered in hypervelocity impact problems), the stability limit is uniquely dependent on the artificial viscosity ν and takes the classical form of the dissipative Courant-Friedrichs-Levy condition:

$$\Delta t \leq \frac{h^2}{2\nu} \, , \qquad \text{or,} \qquad \kappa \leq \frac{1}{2} \, . \tag{71}$$

Remark7. The predictor multi-corrector approach can also be interpreted as a fixed-point iteration procedure [15]. A sufficient condition for the convergence (in spectral space) of such procedure is $\|\boldsymbol{B}_1\| < 1$, that is $\rho(\boldsymbol{B}_1) < 1$. It is not difficult to verify that, when $\beta_k = \pi$, this condition coincides with (67).

7. The case of non-vanishing viscosity

Artificial viscosity operators are usually added in shock hydrodynamics computations to enhance the robustness of the algorithms under extreme shock wave conditions. Viscosity operators usually are modeled as Laplace diffusive operators, and may pose additional constraints on stability, further limiting the time step. In this case, because of the parabolic nature of the problem, the dispersion error analysis is less relevant and is omitted. Also, only results for the conservative scheme are presented, since this method is the main focus of the present work.

7.1. Amplification factor

The amplification factor (spectral radius) of the matrices $\boldsymbol{G}^{(i)}$ is presented as a function of the non-dimensional wave number β_k and acoustic Courant number σ in Figures 2(c), 2(f), 2(i), 2(l), and 2(o), for a value of the non-dimensional viscosity coefficient $\kappa = 1/4$. A comparison with the plots in Figure 2 for the case of $\kappa = 0$ shows that the introduction of diffusion in the proposed predictor/multi-corrector algorithm further restricts the stability range of the even iterates but provides a stability range for the otherwise unstable odd iterates. This fact can more clearly be observed in Figures 8 and 9. Recalling that, by definition and the developments in Section 6, $0 \leq \sigma \leq 1$, and $0 \leq \kappa \leq 1/2$ are necessary for stability, a rearrangement of (67) yields the stability condition:

$$\sigma \leq \sqrt{1 - 2\kappa} \, , \tag{72}$$

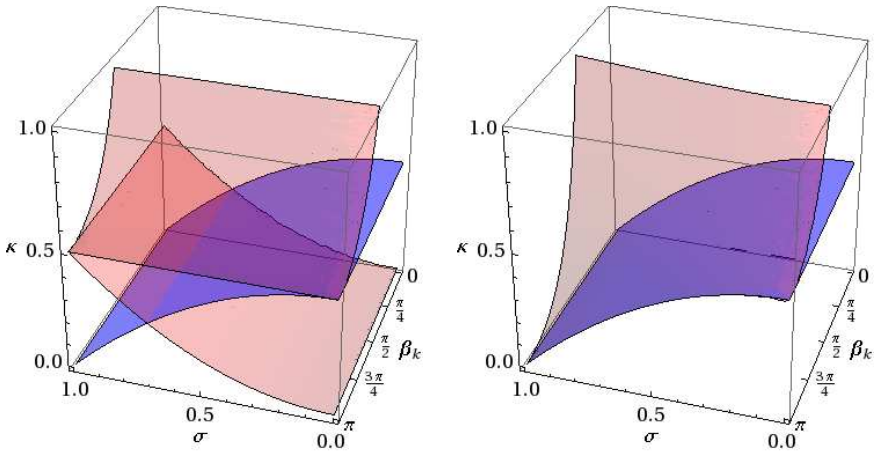

(a) 1st iterate.

(b) 2nd iterate.

(c) 3rd iterate.

(d) 4th iterate.

Figure 11: Three-dimensional (red) surfaces representing the loci of the spectral radii equal to unity for the first four iterates of the conservative predictor/multi-corrector scheme. The blue surfaces represent the stability limit given by (67) (or, equivalently, (69)).

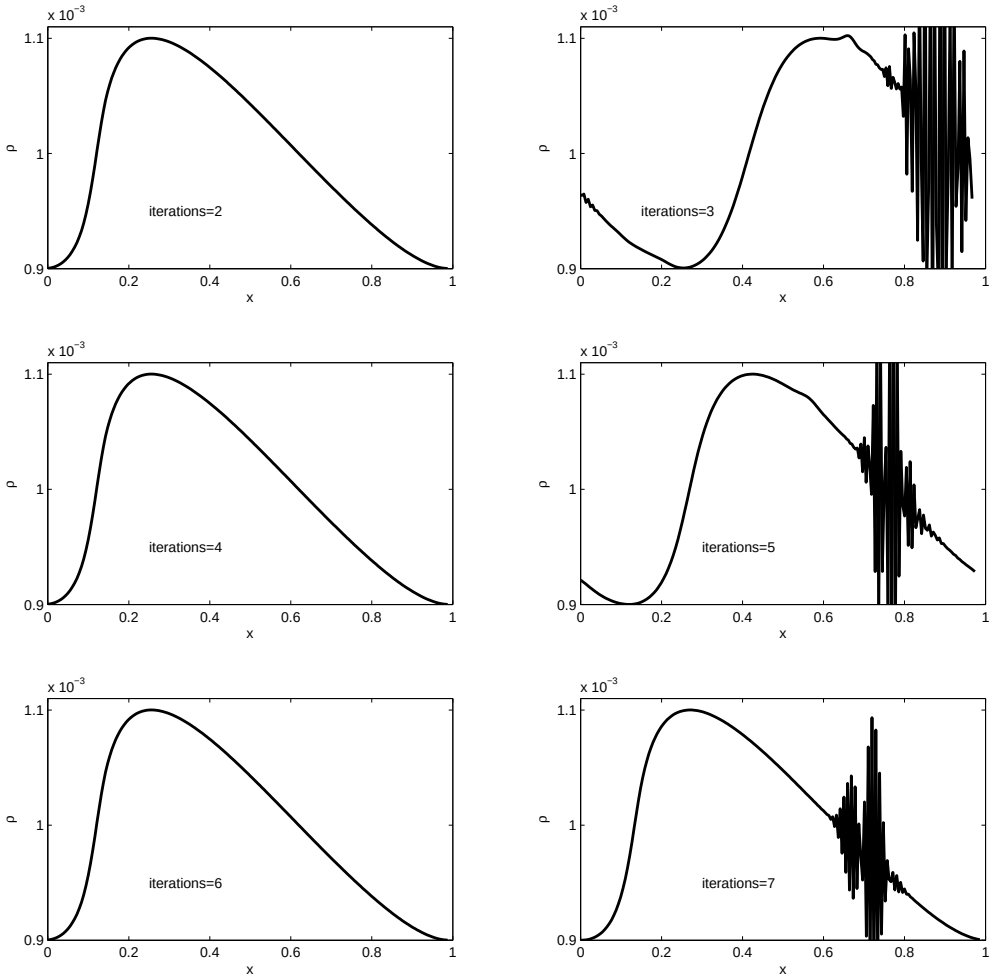

Figure 12: Density versus spatial position at time 2.124×10^{-5} for the periodic breaking wave test problem. Solutions for different number of iterations of the predictor/multi-corrector algorithm are computed with no artificial viscosity and $CFL = 0.90$.

from which, when $\kappa = 1/4$, we obtain $\sigma \leq \sqrt{2}/2 \approx 0.707$. This result can also be verified in Figure 9, for $\beta_k = \pi$. The convergence of the spectral radii of the various iterates to the spectral radius of the implicit case can be evaluated in Figure 10 where sections of the elevation plots of Figure 2 at various values of the parameter σ are presented. Bifurcations of the eigenvalues for the sections at $\sigma = 0.7, 0.8, 0.9$ are clearly visible, although in this case, their effect is not so problematic, because now the original system of partial differential equations has the nature of a wave problem with dissipative damping.

Perhaps the most important plots of this entire article are presented in Figure 11, in which red three-dimensional contour surfaces show the loci of the spectral radii equal to unity for the first, second, third, and fourth iterate of the conservative version of proposed method, in the space $[\sigma, \beta_k, \kappa]$. A blue surface represents the stability limit when equality holds in (67).

Note that in Figures 11(a) and 11(c) the stability region is bounded by two red surfaces. Therefore the presence of diffusion is stabilizing for the first and third iterates, which would otherwise be unstable. The second and forth iterates (Figs. 11(b) and 11(d)) are conditionally stable (at least by visual inspection, since the stability region extends below the red surfaces), with stability condition given by (69)). Hence, in this case, the highest wave numbers seem to impose the most restrictive constraint on the time step.

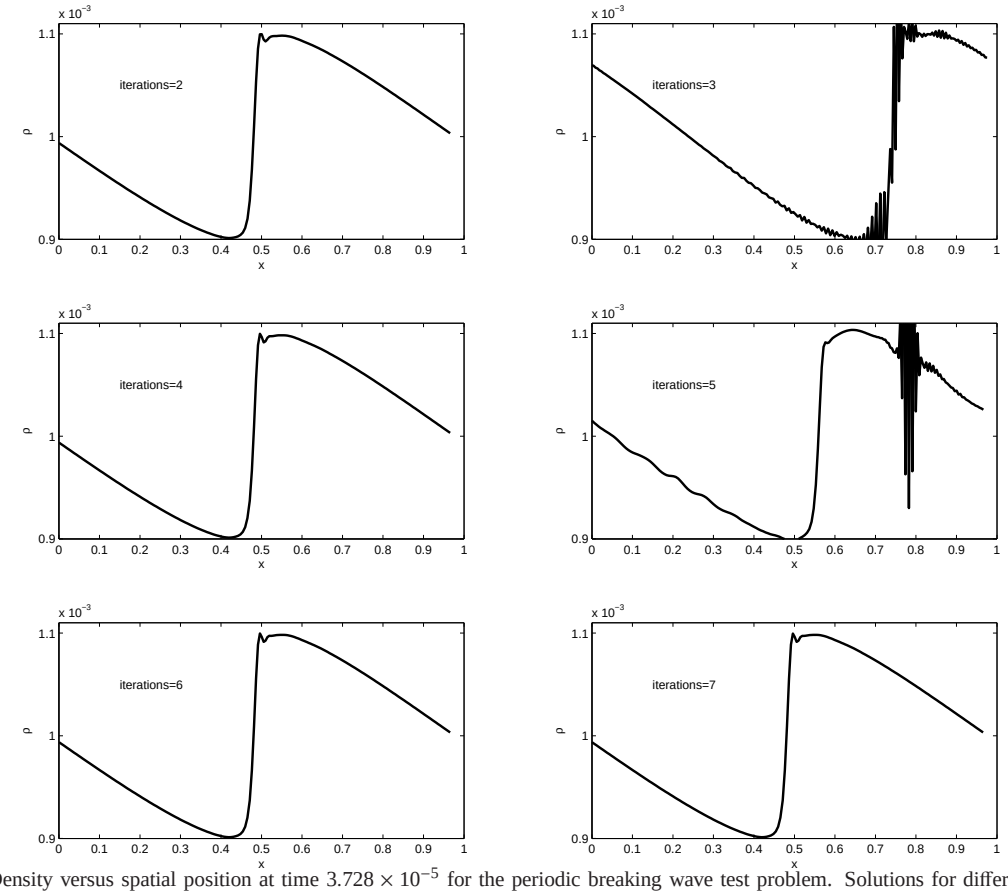

Figure 13: Density versus spatial position at time 3.728×10^{-5} for the periodic breaking wave test problem. Solutions for different number of iterations of the predictor/multi-corrector algorithm are computed with active artificial viscosity and $CFL = 0.90$.

Remark8. The effect of a non-vansihing artificial viscosity is not felt in the truncation error for the phase, which maintains the same order of accuracy as in the undamped case. The truncation error for the dissipation is instead affected, as all iterates do not exceed first-order accuracy, with respect to the undamped wave propagation case.

8. Numerical simulations

We present two tests to show how the time step estimate derived in Section 6 performs.

8.1. Periodic Breaking Wave

An interesting numerical test is represented by a breaking wave problem similar to the one described in [5, 6]. The domain of the problem is the interval $[0, 1]$, subdivided into 200 elements, with periodic boundary conditions. The material is a γ-law ideal gas [10] with $\gamma = 5/3$. The initial density has a sinusoidal variation

$$\rho(x, 0) = 0.001\,(1.0 + 0.1\sin(2\pi x)) \ .$$

The initial pressure is

$$p(x, 0) = 10^6\left(\frac{\rho(x, 0)}{0.001}\right)^{\gamma} ,$$

and the initial velocity is

$$v(x, 0) = 2\frac{(c_{s_0} - c_s)}{\gamma - 1} ,$$

where

$$c_s = \left(\gamma \frac{p(x,0)}{\rho(x,0)}\right)^{1/2},$$

and

$$c_{s_0} = \left(\gamma \frac{10^6}{0.001}\right)^{1/2}.$$

The solution is smooth for a finite time $0 < T_{\text{break}} < \infty$, at which point the wave breaks and a shock forms [5, 6]. The nonlinear version of the present algorithm, described in detail in [14, 15], is used. The results of Figure 12 are obtained for several predictor/multi-corrector iterates, with no viscosity applied. The results of Figure 13 are obtained with coefficients for the linear and quadratic part of the nonlinear artificial viscosity chosen as $c_1 = 0.15$ and $c_2 = 2.0$, respectively. All simulations were run using $CFL = 0.90$. Consistent with the preceding analysis, an even number of iterations appears to be stable. An odd number of iterations produces unstable results when no artificial viscosity is applied, but stability is regained in the case of 7 iterations when the artificial viscosity is active. This may be the result of the convergence of the predictor/multi-corrector algorithm in combination with the dissipation produced by the artificial viscosity. In practical computations, however, one cannot expect the artificial viscosity to be active everywhere in the computational domain.

8.2. Interacting Blast Waves

As a second numerical test, we consider the Woodward-Colella interacting shock wave test problem [19]. In one dimension the domain of the problem is the interval $[0, 1]$, subdivided into 400 elements. Again, the material is a γ-law ideal gas with $\gamma = 1.4$. The gas is initially at rest between reflecting walls, with a uniform initial density everywhere equal to 1. On the subdomain $[0, 0.1]$ the initial pressure is 1000 and on the subdomain $[0.9, 1.0]$ the initial pressure is 100. Everywhere else the pressure is initialized to 0.01. Two strong shock waves develop and interact. The linear and quadratic part of the nonlinear artificial viscosity have coefficients $c_1 = 0.15$ and $c_2 = 2.0$, respectively. Figure 14 plots the numerical results of density versus position for various values of the CFL control parameter. Two predictor/corrector iterations are used for these simulations. The simulations with $CFL \leqslant 1$ do not show any sign of instability, while the simulations with $CFL > 1.10$ appear mildly unstable. The time step stability estimate seems to be accurate (and more restrictive) to within about 10%, at least for this test problem.

Remark9. This added stability may be due to the conservation properties enjoyed by the algorithm in the nonlinear setting, which bound the global total energy to stay constant throughout the computation.

Remark10. The large spurious overshoot in density at $x \approx 0.765$ is typical of Lagrangian simulations of this test [9, 12], and is a somewhat expected feature in this computation.

9. Summary

We have presented a von Neumann stability analysis of a linearized version of the predictor/multi-corrector algorithm proposed in [14, 15], which, at least in the one-dimensional setting, coincides with the time integrators documented in [2, 4]. We have highlighted as a curious feature of this algorithm, that the odd iterates are unconditionally unstable, while the even are conditionally stable (at least up to four iterates). Numerical test showed that the time-step stability bound derived in the linearized analysis works well also in the nonlinear case.

Acknowledgments

The authors would like to thank, for very valuable discussions, Professor T. J. R. Hughes at the University of Texas in Austin, Dr. M. Shashkov at Los Alamos National Laboratory, and Dr. C. Ober, Dr. T. Voth, Dr. V. G. Weirs, and Dr. M. Wong at Sandia National Laboratories. The authors would also like to thank Dr. R. Summers and Dr. S. Collis, at Sandia National Laboratories, for support and encouragement during the development of this research work.

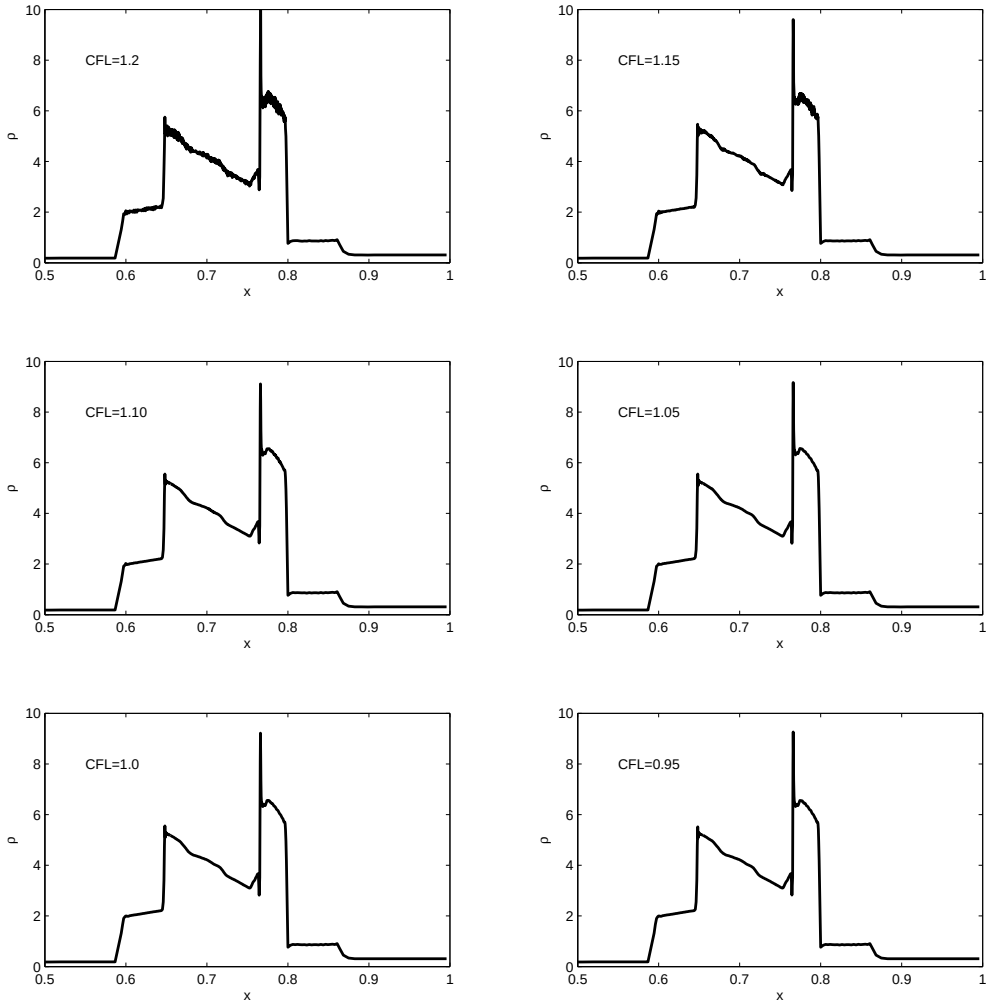

Figure 14: Density versus spatial position for the Woodward-Colella test problem for incrementally decreasing values of the *CFL* parameter. Plots are at the final time of 0.038.

References

[1] M. L. Abell and J. P. Braselton. *Mathematica by Example*. Academic Press, 4th edition, 2008.

[2] A. Barlow. A compatible finite element multi-material ALE hydrodynamics algorithm. *International Journal for Numerical Methods in Fluids*, **56**(8):953–964, 2008.

[3] A. Bauer, R. Loubère, and B. Wendroff. On stability of staggered schemes. *SIAM Journal on Numerical Analysis*, **46**(2):996–1011, 2008.

[4] E. J. Caramana, M. J. Shashkov, and P. P. Whalen. Formulations of artificial viscosity for multi-dimensional shock wave computations. *Journal of Computational Physics*, **144**:70–97, 1998.

[5] A. W. Cook and W. H. Cabot. A high-wavenumber viscosity for high-resolution numerical methods. Technical Report UCRL-ID-152002, Lawrence Livermore National Laboratory, Livermore, CA, 2003.

[6] A. W. Cook and W. H. Cabot. A high-wavenumber viscosity for high-resolution numerical methods. *Journal of Computational Physics*, **195**(2):594–601, 2004.

[7] A. Curnier. *Computational Methods in Solid Mechanics*. Kluwer Academic Press, Amsterdam, 1994.

[8] R. A. Horn and C. R. Johnson. *Matrix Analysis*. Cambridge University Press, Cambridge, UK, 1985.

[9] R. Loubère and M. J. Shashkov. A subcell remapping method on staggered polygonal grids for arbitrary-lagrangian eulerian methods. *Journal of Computational Physics*, **209**(1):105–138, 2005.

[10] R. Menikoff and B. J. Plohr. The Riemann problem for fluid flow of real materials. *Reviews of Modern Physics*, **61**(1):75–130, 1989.

[11] A. R. Mitchell and D. F. Griffiths. *The Finite Difference Method in Partial Differential Equation*. John Wiley, London, 1980.

[12] R. B. Pember and R. W. Anderson. Comparison of staggered-mesh lagrange plus remap and cell-centered direct eulerian godunov schemes for eulerian shock hydrodynamics. Technical Report UCRL-JC-139820, Lawrence Livermore National Laboratory, Livermore, CA, November 2000.

[13] G. Scovazzi. Stabilized shock hydrodynamics: III. A new stabilization concept for Lagrangian Computations. Computer Methods in Applied Mechanics and Engineering, 2009. Submitted.

[14] G. Scovazzi, E. Love, and M. J. Shashkov. A multi-scale Q1/P0 approach to Lagrangian shock hydrodynamics. Technical report, SAND2007-1423, Sandia National Laboratories, New Mexico, March 2007. Available at: `http://www.cs.sandia.gov/~gscovaz`.

[15] G. Scovazzi, E. Love, and M. J. Shashkov. A multi-scale Q1/P0 approach to Lagrangian shock hydrodynamics. *Computer Methods in Applied Mechanics and Engineering*, **197**(9–12):1056–1079, 2008.

[16] G. Scovazzi, J. N. Shadid, E. Love, and T. J. R. Hughes. Stabilized shock hydrodynamics: IV. Computations with a conservative updated Lagrangian method. Computer Methods in Applied Mechanics and Engineering, 2009. Submitted.

[17] J. C. Strikwerda. *Finite Difference Schemes and Partial Differential Equations*. Chapman & Hall, New York, 1989.

[18] S. Wolfram. *The Mathematica Book*. Cambridge University Press, 4th edition, 1999.

[19] P. R. Woodward and P. Colella. The numerical simulation of two-dimensional fluid flow with strong shocks. *Journal of Computational Physics*, **54**:115–173, 1984.